Materials Today Communications 53 (2026) 115301

Contents lists available at ScienceDirect

Materials Today Communications

journal homepage: www.elsevier.com/locate/mtcomm

# Enhanced performance of $Sb_2Se_3$-based solar cells with Fe doped $CuGa(S,Te)_2$ as a secondary absorber

Danial Keighobadi [a], Ali Asghar Orouji [a], Mehdi Mousavi-Kamazani [b], Mohammad Danaie [a,*]

[a] Faculty of Electrical and Computer Engineering, Semnan University, Semnan, Iran
[b] Department of Nanotechnology, Faculty of New Sciences and Technologies, Semnan University, Semnan, Iran

ARTICLE INFO

*Keywords:*
$Sb_2Se_3$ solar cells
Thin-film solar cells
Fe doped
CuGa(S,Te)2 absorber
Dual Absorber structure
High-performance solar cells design

ABSTRACT

This study proposes a dual-absorber $Sb_2Se_3$-based solar cell incorporating Fe-doped $CuGa(S,Te)_2$ (Fe-CGST) as a secondary absorber layer. A systematic thickness optimization of both absorber layers is performed, identifying 2.6 $\mu$m for $Sb_2Se_3$ and 400 nm for Fe-CGST as optimal values. The introduction of an intermediate band (IB) through Fe doping enables sub-bandgap photon absorption, enhancing carrier generation and spectral utilization. The optimized device demonstrates significant improvements in key photovoltaic parameters, including open-circuit voltage ($V_{oc}$), short-circuit current density ($J_{sc}$), fill factor (FF), and overall efficiency ($\eta$). A maximum efficiency of 18.54% is achieved, compared to 10.12% for the conventional structure. Detailed optoelectronic analysis, including EQE, capacitance–voltage (C-V), and Nyquist characteristics, reveals improved charge transport, reduced recombination losses, and enhanced carrier collection efficiency. These findings highlight the effectiveness of combining dual-absorber design with intermediate band engineering for high-performance thin-film solar cells.

## 1. Introduction

Solar cells are a cornerstone technology in the global pursuit of sustainable and environmentally friendly energy solutions [1–5]. This technology offers an innovative and environmentally friendly approach to addressing the energy crisis by converting sunlight into electrical energy [6,7].

Among various photovoltaic candidates, thin-film solar cells based on materials such as $Sb_2Se_3$ have attracted significant attention due to their suitable optoelectronic properties and potential for high-efficiency device architectures [8–19]. Within the realm of narrow-bandgap absorbers, Antimony Selenide ($Sb_2Se_3$) has garnered significant attention. With an optimal bandgap energy ($E_g$) of approximately 1.2 eV, $Sb_2Se_3$ demonstrates excellent absorption in the visible and near-infrared regions, positioning it as a highly promising material for the bottom cell component in multi-junction devices. Additionally, this material exhibits excellent chemical and physical stability, which enhances the lifespan of solar cells and provides resistance to degradation from prolonged solar irradiation [18,20–22].

The use of $Sb_2Se_3$ in solar cells offers several advantages. One key benefit is its ability to reduce the cost of solar cell production, owing to the simpler and more cost-effective fabrication processes involved in producing $Sb_2Se_3$ as an absorber. Moreover, $Sb_2Se_3$ exhibits excellent compatibility with other materials such as CdS and ZnO, which results in improved performance and efficiency of the solar cells [23–25]. Furthermore, $Sb_2Se_3$ demonstrates good resistance to environmental factors, including temperature and humidity, making it suitable for use in a variety of environmental conditions [26–30].

The use of dual-absorber configurations has been widely proposed as an effective strategy to enhance spectral utilization and improve device performance in thin-film solar cells, including $Sb_2Se_3$ -based structures [31–34]. In this configuration, $Sb_2Se_3$ acts as the primary absorber, efficiently capturing a broad range of light from the visible and near-infrared spectrum. This dual-absorber combination effectively covers all important wavelengths, allowing the solar cell to absorb lighter and convert it into electrical energy, leading to improved overall cell efficiency [12,29,35].

Recent advances in defect engineering have opened new avenues for optimizing light harvesting. In particular, the incorporation of foreign elements into semiconductor lattices can introduce intermediate energy states within the bandgap. $CuGa(S,Te)_2$ (CGST), as a tunable wide-bandgap semiconductor, has attracted considerable attention due to

* Corresponding author.
*E-mail address:* danaie@semnan.ac.ir (M. Danaie).

https://doi.org/10.1016/j.mtcomm.2026.115301
Received 13 February 2026; Received in revised form 25 April 2026; Accepted 29 April 2026
Available online 1 May 2026

its favorable optoelectronic properties and compatibility with high-efficiency device architectures [8,30,36–40].

For instance, Vijayan et al. [41]. demonstrated that Fe doping in CGST with an optimized concentration (∼0.08 at%) leads to the formation of an intermediate band (IB) within the bandgap. This IB enables sub-bandgap photon absorption through a two-step transition mechanism, thereby enhancing carrier generation and improving device performance. The selection of this doping level is based on its ability to introduce stable intermediate energy states while minimizing recombination losses and preserving the structural integrity of the material.

The presence of the intermediate band plays a crucial role in improving the optoelectronic performance of the device. By enabling additional absorption pathways, the IB allows photons with energies lower than the bandgap to contribute to carrier generation. This results in an enhanced photocurrent and improved spectral utilization, particularly in wavelength regions where $Sb_2Se_3$ alone exhibits limited absorption.

In light of these promising individual advancements, the present study focuses on capitalizing on the synergistic effects between these two disparate, yet complementary, absorbers. We propose and thoroughly analyze the photovoltaic performance of a novel two-absorber thin film solar cell adopting the structure: $Sb_2Se_3$/Fe-CGST/CdS/ZnO/AlZnO. In this configuration, the IB-enabled Fe-CGST functions as the wide-bandgap absorber for the top layer, while the narrow-bandgap $Sb_2Se_3$ is utilized as the absorber layer for the bottom layer. By integrating the spectral utilization capabilities of the IB material with the broad absorption of $Sb_2Se_3$, we aim to demonstrate a technologically viable and highly stable architecture suitable for commercial applications, while addressing efficiency limitations and stability challenges reported in previous studies [1–3,41]. The objective of this work is to achieve superior current matching and an overall power conversion efficiency ($\eta$) significantly higher than that achievable by single-junction devices [12,29,35,42–48]. In addition, a systematic thickness optimization of both absorber layers ($Sb_2Se_3$ and Fe-CGST) is performed to achieve the optimal device performance.

## 2. The proposed dual absorber solar cell

In this section, the new structure and conventional structure (Ref. [11]) of $Sb_2Se_3$ based solar cells are examined and compared. The new structure incorporates *Fe-CGST* as a secondary absorber layer, which plays a crucial role in improving light absorption and increasing the efficiency of the solar cells. In Fig. 1(a), the new structure is shown, where different layers are clearly represented, with *Fe-CGST* highlighted as the secondary absorber layer. This structure includes the layers *AlZnO, ZnO, CdS, Fe-CGST*, $Sb_2Se_3$, $MoSe_2$, and *Mo*. In this configuration, *Fe-CGST* effectively captures light at wavelengths that $Sb_2Se_3$ cannot absorb, leading to an overall improvement in solar cell performance.

In Fig. 1(b), the conventional structure of $Sb_2Se_3/CdS/ZnO/AlZnO$ is shown, which lacks the secondary absorber layer and only uses $Sb_2Se_3$, *CdS*, *ZnO*, and *AlZnO* materials. This structure typically has a more limited capacity to absorb light from certain parts of the spectrum and thus exhibits lower efficiency compared to the new structure. As illustrated in the proposed structure and energy band diagram, the incorporation of Fe-CGST is expected to improve device performance through enhanced spectral utilization and more favorable band alignment. Thus, the comparison of these two structures can be more clearly understood in terms of their material properties and optical behavior. $Sb_2Se_3$, with its narrow bandgap (∼1.1 eV), efficiently absorbs photons in the visible and near-infrared regions, while Fe-CGST, with a wider bandgap (∼1.9 eV), is more effective in absorbing higher-energy photons. This complementary bandgap configuration allows for improved spectral utilization, where each absorber contributes to different regions of the solar spectrum. In addition, the higher absorption coefficient of Fe-CGST in specific wavelength ranges enhances overall light harvesting. Furthermore, the integration of these materials improves charge carrier generation and reduces recombination losses through better band alignment and carrier transport properties. As a result, the dual-absorber structure provides a more efficient and physically optimized approach for enhancing solar cell performance compared to the conventional single-absorber design.

In this section, the differences between the new structure ($Sb_{2Se_3}/Fe-CGST/CdS/ZnO/AlZnO$) (Fig. 2(a)) as a secondary absorber layer and the conventional $Sb_2Se_3/CdS/ZnO/AlZnO$ structure (Fig. 2(b)) are examined from the perspective of the energy band diagram. In the new structure, Fe-CGST is highlighted as a secondary absorber layer, contributing to improved device performance through favorable band alignment and enhanced charge carrier separation. The optical absorption characteristics are more clearly discussed in Section 4, where the absorption coefficients of the materials are presented.

The *Fe-CGST*, with its unique optical properties, is capable of absorbing light in parts of the spectrum that $Sb_2Se_3$ cannot capture. This

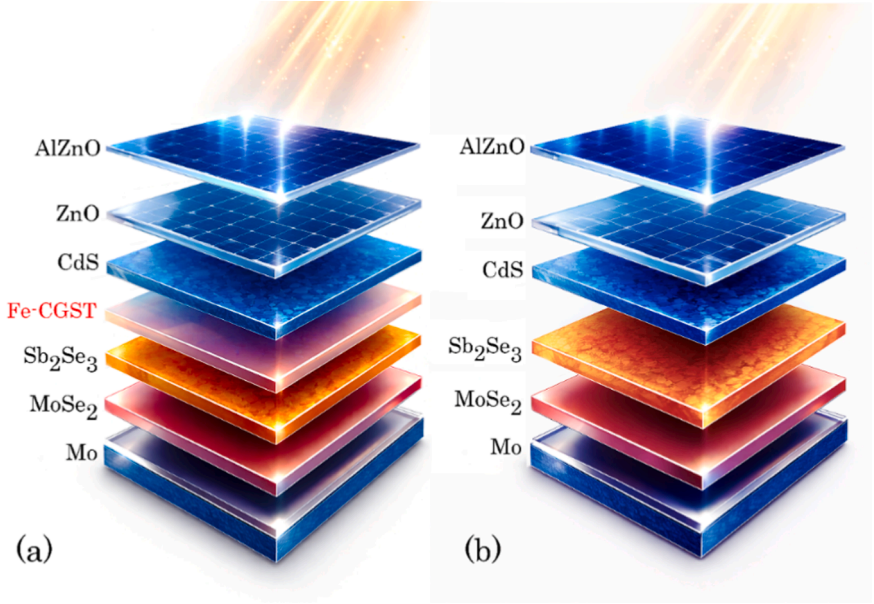


**Fig. 1.** Comparison of the new $Sb_2Se_3$ solar cell structure (a), with Fe-CGST as a secondary absorber layer and (b), the conventional structure [11].

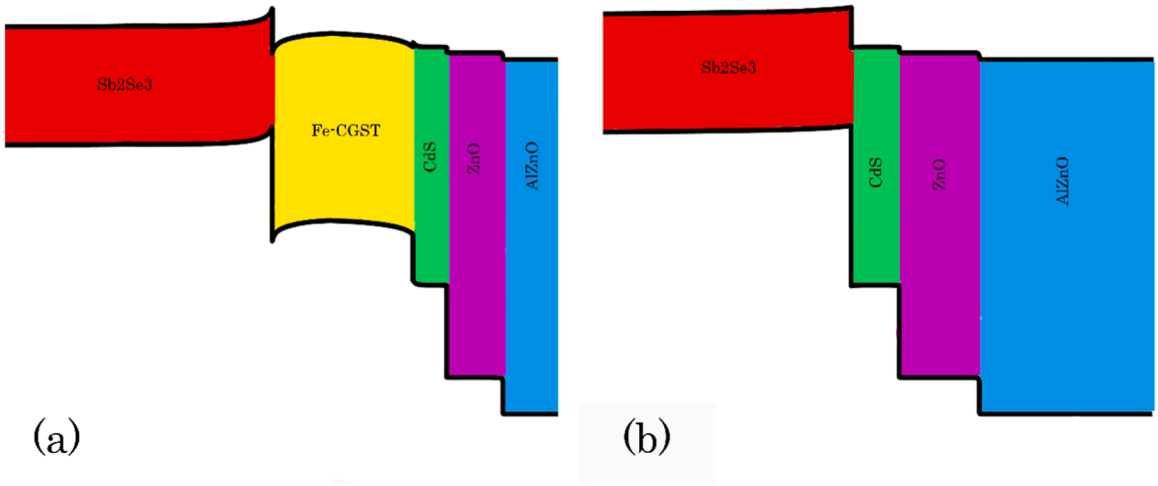


**Fig. 2.** (a), Energy band diagram for the new $Sb_2Se_3$ structure with Fe-CGST as the secondary absorber layer. (b), Energy band diagram for the conventional $Sb_2Se_3$/CdS/ZnO/AlZnO structure [11].

characteristic allows the *Fe-CGST* to more effectively capture sunlight, which directly leads to an increase in the overall efficiency of the solar cells.

The energy band diagram in the new structure demonstrates a reduction in the bandgap and better alignment between the energy bands of the layers. These changes directly affect the cell's performance, leading to increased light absorption and higher energy conversion efficiency. In contrast, in the conventional structure,$Sb_2Se_3$ functions solely as the absorber, and its wider bandgap limits the solar cell's ability to utilize the full potential of the solar spectrum. In this structure, the band alignment is more constrained, and the light absorption efficiency is reduced for certain parts of the spectrum.

One of the key features in the new structure is the concept of cumulative light intensity function (CLIF), which is used here as a qualitative representation of the cumulative absorption of incident photons across the solar spectrum. CLIF does not represent a separate physical parameter, but rather reflects the integrated light absorption behavior of the device.

The incorporation of Fe-CGST as a secondary absorber layer enhances spectral utilization by enabling absorption over a wider wavelength range. This effect can be qualitatively understood through CLIF, while the actual improvement in device performance is more directly confirmed by EQE and current density results.

Overall, the changes introduced in the new structure, both in terms of bandgap reduction and the improvement in CLIF, represent a substantial enhancement in the performance of the solar cells, which can lead to improved stability, efficiency, and longevity of solar cells in commercial-scale applications.

## 3. Calibration and validation

In this section, the simulation results obtained using the SCAPS software for the $Sb_2Se_3$ solar cell structure are compared and validated against previously reported experimental data from the literature (Ref. [11]). SCAPS is an advanced simulation tool used for modeling the behavior of thin-film solar cells. The software provides accurate simulations of the electrical, optical, and thermodynamic properties of semiconductor materials, which directly aids in evaluating and predicting the performance of solar cells. It should be noted that the experimental data used in this study were not obtained by the authors but were adopted from Ref. [11] for validation purposes.

The simulation performed using SCAPS for the $Sb_2Se_3$ solar cell structure accurately predicted the efficiency and performance characteristics of the cells. In Fig. 3(a), which shows the simulated External Quantum Efficiency (EQE) and Integrated $J_{sc}$ results are compared with experimental data. The simulation accurately reproduced the EQE results, demonstrating the high reliability of the model in simulating the optical response of the solar cell. Additionally, Fig. 3(b), which shows the current density versus voltage, exhibits a high degree of agreement between the simulated and experimental data. This agreement indicates

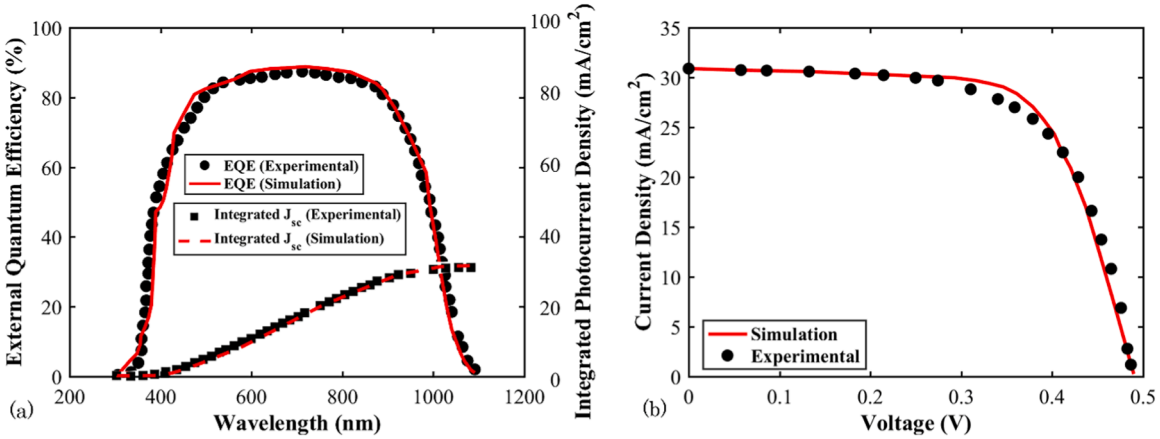


**Fig. 3.** Comparison of simulation results with experimental data from Ref [11]. for (a) External Quantum Efficiency (EQE) and integrated photocurrent density, and (b) current density versus voltage (J–V) characteristics.

the accuracy of the simulation in modeling the electrical behavior of the solar cells.

Validating the simulation results with experimental data is particularly crucial for key parameters like current density and open-circuit voltage ($V_{oc}$), as these are primary indicators of solar cell performance. The precise matching of these values in both the simulations and experiments confirms that SCAPS has effectively modeled the functional characteristics of the cells. Moreover, the experimental data, in comparison with the simulations, demonstrate the stability and high precision of the model, which is especially beneficial for predicting outcomes at the industrial scale.

This validation not only confirms the accuracy of the simulations but also paves the way for utilizing this software in predicting the performance of new solar cells and improving cell structures. Thus, the simulations carried out using SCAPS will effectively contribute to enhancing the design and development of solar cells with higher performance and greater efficiency.

## 4. Simulation results and discussions

Prior to analyzing the device performance, a systematic thickness optimization of both the $Sb_2Se_3$ and Fe-CGST absorber layers was carried out. The selected absorber thicknesses are within the typical range of thin-film photovoltaic devices and are consistent with physically realistic values reported in the literature. In such devices, the absorber thickness is governed by a trade-off between optical absorption and carrier transport, where excessively thin layers limit photon absorption, while overly thick layers introduce recombination losses and transport limitations. This behavior is consistent with established thin-film device physics and experimentally relevant thickness ranges [49].

The optimal thickness values were determined to be 2.6 μm for $Sb_2Se_3$ and 400 nm for Fe-CGST, based on achieving the highest efficiency and balanced optoelectronic performance. All subsequent optoelectronic analyses, including EQE, C-V, and Nyquist characteristics, are based on this optimized device configuration. The enhancement in light absorption is more clearly illustrated in Fig. 4, which presents the absorption coefficients of the materials used in the device. In Fig. 4, the absorption coefficient for various materials used in the proposed structure is presented.

The absorption characteristics of Fe-CGST are based on reported literature data, while the parameters for other materials are obtained from standard SCAPS databases and commonly reported values. These wavelength-dependent absorption coefficients are directly used as input in SCAPS simulations to model optical generation within the device. Since SCAPS requires absorption coefficient data as a primary optical input, the use of absorption spectra is more appropriate than transmission spectra for device-level simulation and analysis.

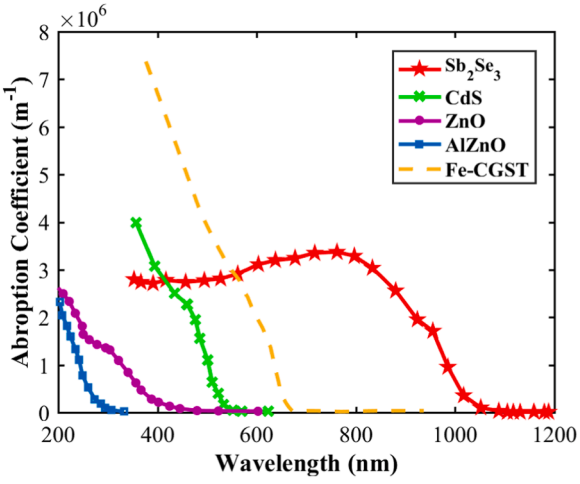


**Fig. 4.** Comparison of the absorption coefficients of various materials used in the proposed solar cell. The absorption data for Fe-CGST are taken from Ref. [41], while the parameters for other materials are based on SCAPS database and literature values.

*The Fe-CGST*, as a multi-absorber compound with distinct optical characteristics, exhibits high absorption capabilities in wavelength regions that are less effectively absorbed by other materials in the conventional structure. Specifically, Fe-CGST as a secondary absorber layer contributes to improved spectral utilization through both direct bandgap absorption in the visible region and intermediate band-assisted sub-bandgap absorption in the mid-to-long wavelength range, where $Sb_2Se_3$ and *CdS* show limited absorption. This property allows *Fe-CGST* to more effectively absorb sunlight, directly contributing to the increased efficiency of the solar cells.

In comparison to $Sb_2Se_3$ as the primary absorber, which predominantly absorbs light in shorter wavelengths (below 600 nm), Fe-CGST enhances the overall spectral response by contributing to absorption in higher-energy regions and, through intermediate band (IB) effects, enabling sub-bandgap photon utilization. This feature makes *Fe-CGST* a highly complementary absorber for $Sb_2Se_3$, enabling the solar cell to capture a broader spectrum of sunlight and ultimately improve the energy conversion efficiency.

When compared to other materials in the conventional structure, such as *CdS* and *ZnO*, which have absorption coefficients mostly confined to specific parts of the spectrum, *Fe-CGST* extends the light absorption into the higher wavelength regions, from 600 nm onward. While *CdS* and *ZnO* are effective primarily in the short and mid-wavelength ranges, *Fe-CGST* plays a significant role in the absorption of longer wavelengths, providing a broader and more efficient absorption profile.

Overall, the inclusion of *Fe-CGST* as a secondary absorber layer significantly increases the absorption coefficient in various parts of the spectrum, leading to higher efficiency and a more effective use of sunlight. These unique properties of *Fe-CGST* result in a substantial improvement in the performance of the solar cells compared to the conventional structure, ultimately enhancing solar cell efficiency and overall system performance.

Table 1, presents a detailed comparison of the material and electrical parameters for the proposed solar cell structure and the reference solar cell structure based on the work of [11]. The comparison covers the key characteristics of the $Sb_2Se_3$/*Fe-CGST/ CdS/ZnO/AlZnO* materials used in the solar cells, as well as their respective electrical and material properties.

The $Sb_2Se_3$ layer, with a thickness of 2.6 $\mu$m, is utilized as the primary absorber in the proposed cell, exhibiting an energy bandgap ($E_g$) of 1.1 eV, which is optimized for absorbing visible light. In contrast, Fe-CGST, the secondary absorber layer, has a bandgap of 1.9 eV, making

**Table 1**
Comparison of material and electrical parameters for proposed and the reference solar cell structures [11,41].

| Parameter | $Sb_2Se_3$ | $Fe-CGST$ | $CdS$ | $ZnO$ | $ZnO$-$Al$ |
|---|---|---|---|---|---|
| Thickness ($\mu m$) | 2.6 | 0.4 | 0.06 | 0.1 | 0.3 |
| $E_g$ (eV) | 1.1 | 1.9 | 2.42 | 3.3 | 3.6 |
| $\chi_e$ (eV) | 4.16 | 4.5 | 4.45 | 4.5 | 4.5 |
| $\varepsilon_r$ | 18.9 | 13 | 10 | 9 | 9 |
| $N_c$ ($1/cm^3$) | $1 \times 10^{19}$ | $1.2 \times 10^{18}$ | $2.2 \times 10^{18}$ | $2.2 \times 10^{18}$ | $2.2 \times 10^{18}$ |
| $N_V$ ($1/cm^3$) | $1 \times 10^{19}$ | $1.8 \times 10^{19}$ | $1.8 \times 10^{19}$ | $1.8 \times 10^{19}$ | $1.8 \times 10^{19}$ |
| $\mu_e$ ($cm^2/V{\cdot}s$) | 15 | 100 | 100 | 100 | 100 |
| $\mu_h$ ($cm^2/V{\cdot}s$) | 5.1 | 25 | 25 | 25 | 25 |
| Doping ($1/cm^3$) | $6.9 \times 10^{15}$ | $1.2 \times 10^{15}$ | $7.12 \times 10^{17}$ | $1 \times 10^{18}$ | $1 \times 10^{20}$ |
| Function | Absorber | Absorber | Buffer | ETL | TCO/ ETL |

it more effective in absorbing higher-energy photons. In addition, the incorporation of Fe introduces an intermediate band (IB) within the bandgap, enabling sub-bandgap photon absorption through a two-step excitation mechanism. This allows lower-energy photons to contribute to carrier generation, thereby enhancing spectral utilization beyond the intrinsic bandgap limitation.

The *CdS* buffer layer, with a thickness of 0.06 $\mu$m, and the *ZnO* and Al*ZnO* layers serve as electron transport layers (ETL) and transparent conductive oxides (TCO), respectively.

In terms of electrical properties, the $Sb_2Se_3$ layer has an electron affinity ($\chi_e$) of 4.16 eV, which ensures good alignment with the *Fe-CGST* and *CdS* layers for efficient charge separation. The electron mobility ($\mu_e$) and hole mobility ($\mu_h$) for $Sb_2Se_3$ are 15 $Cm^2/V{\cdot}s$ and 5.1 $Cm^2/V{\cdot}s$, respectively, reflecting its relatively good charge transport properties compared to *Fe-CGST*, which has higher electron mobility of 100 $Cm^2/V{\cdot}s$. The band alignment between the layers plays a critical role in determining device performance. The incorporation of Fe-CGST modifies the conduction and valence band offsets at the interfaces, leading to more favorable charge transport conditions. In particular, the conduction band offset at the Fe-CGST/CdS interface is reduced, facilitating electron transport, while the valence band alignment helps suppress hole recombination.

This improved interface quality reduces recombination losses and contributes to the enhancement in open-circuit voltage (Voc) and overall device efficiency observed in the proposed structure.

The doping concentration for the materials ranges from $6.9 \times 10^{15} cm^{-3}$ for $Sb_2Se_3$ to $1 \times 10^{20} cm^{-3}$ for *AlZnO*, showing the level of conductivity in each material. The *ZnO* layer, with a doping concentration of $1 \times 10^{18} cm^{-3}$, plays a crucial role in enhancing the electron collection at the interface with the absorber layers, while the *AlZnO* layer serves as the final electron transport layer, contributing to improved overall conductivity.

This detailed comparison underscores the significant role of the *Fe-CGST* layer as a secondary absorber in improving the performance of the proposed solar cell structure. The choice of materials and their specific properties contribute to enhanced light absorption, charge separation, and transport efficiency, leading to the high-efficiency performance observed in the simulations. The synergy between these layers provides a promising foundation for developing high-performance solar cells with better overall efficiency and stability.

In this Fig. 5, the current density versus voltage for the proposed cell and reference cell is compared. The proposed cell, which incorporates the *Fe-CGST* as a secondary absorber layer, exhibits an open-circuit voltage ($V_{oc}$) of 0.77 V and a short-circuit current density ($J_{sc}$) of 34.50 $mA/cm^2$. The fill factor (FF) is 69.25%, and the efficiency ($\eta$) is 18.54%. In contrast, the reference cell shows an open-circuit voltage ($V_{oc}$) of 0.48 V, with a short-circuit current density ($J_{sc}$) of 30.87 $mA/cm^2$, resulting in a lower fill factor (FF) of 67.18% and an efficiency ($\eta$) of 10.12% [11].

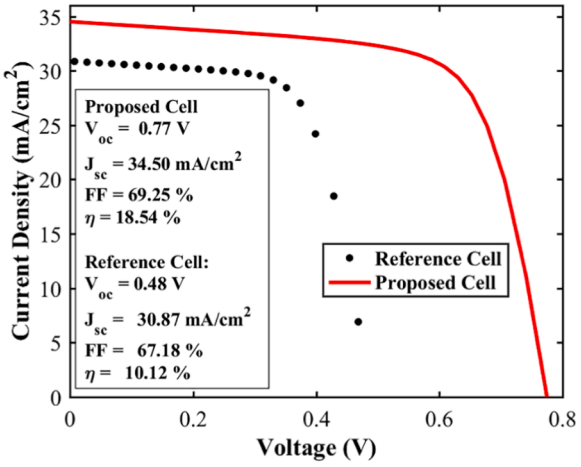


**Fig. 5.** Comparison of current density versus voltage for the proposed cell and the reference cell. The proposed cell shows higher open-circuit voltage and efficiency.

The observed improvement in device performance can be explained by several underlying physical mechanisms. The increase in short-circuit current density ($J_{sc}$) is primarily attributed to enhanced light absorption resulting from the inclusion of the Fe-CGST secondary absorber layer, which extends the spectral response of the device. This effect is consistent with the improved EQE observed in Fig. 7, particularly in the longer wavelength region.

The enhancement in open-circuit voltage ($V_{oc}$) can be associated with improved band alignment and an increase in the built-in potential, as confirmed by the Schottky analysis (Fig. 6). This leads to more efficient charge separation and reduced recombination losses.

Moreover, the improvement in fill factor (FF) is linked to better charge transport and reduced internal resistance, as evidenced by the Nyquist plot (Fig. 8), which shows lower charge transfer resistance in the proposed structure. These combined effects result in a significant enhancement in the overall efficiency of the solar cell.

This comparison clearly demonstrates the superior performance of the proposed cell that utilizes *Fe-CGST* as the secondary absorber layer. The substantial differences in $V_{oc}$ and $J_{sc}$, along with the higher efficiency, indicate that incorporating *Fe-CGST* into the solar cell structure directly enhances its performance. The proposed cell with *Fe-CGST* as the secondary absorber layer shows improved light absorption and energy conversion efficiency.

These findings highlight the effectiveness of *Fe-CGST* as a secondary absorber layer for improving solar cell performance, resulting in higher efficiency and greater stability.

It is important to note that Fe-CGST is not intended to function as a standalone absorber layer in this study. Due to its relatively wide bandgap (~1.9 eV), Fe-CGST alone cannot effectively absorb the full solar spectrum, particularly in the longer wavelength region. Therefore, its performance as a single absorber is expected to be limited.

In contrast, when combined with $Sb_2Se_3$ in a dual-absorber configuration, Fe-CGST plays a complementary role by extending spectral absorption and enabling intermediate band-assisted carrier generation. This synergistic effect leads to improved overall device performance compared to single-absorber configurations.

The Mott-Schottky plot in Fig. 6, compares the $Sb_2Se_3$ solar cells with

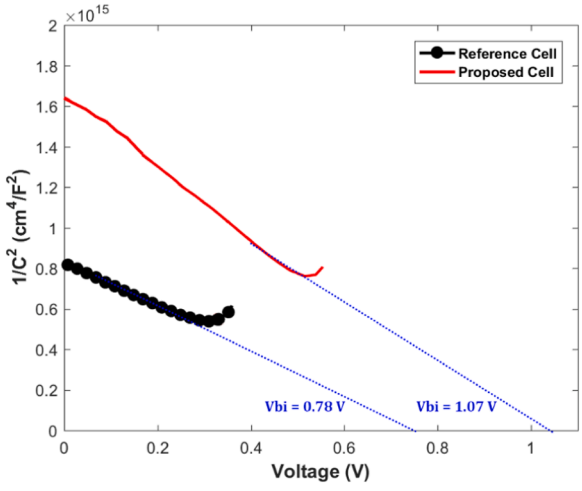


**Fig. 6.** Mott-Schottky plot comparing $Sb_2Se_3$ solar cells with Fe-CGST as the secondary absorber layer and the conventional $Sb_2Se_3$/CdS/ZnO/AlZnO structure. This plot illustrates the comparison of $1/C^2$ versus voltage for investigating the built-in voltage ($V_{bi}$) and band bending characteristics.

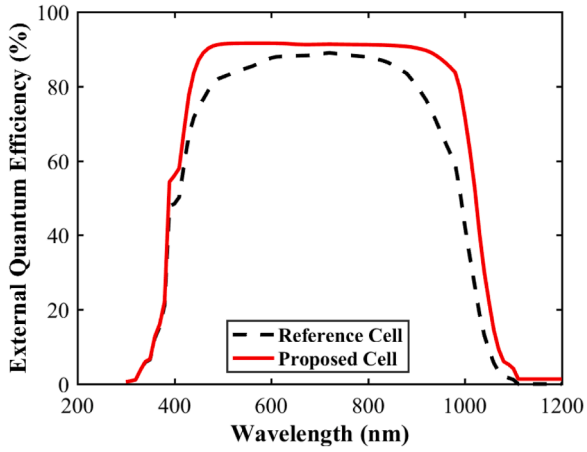


**Fig. 7.** Comparison of External Quantum Efficiency (EQE) versus wavelength for the proposed cell with the Fe-CGST as the secondary absorber layer and the conventional cell.

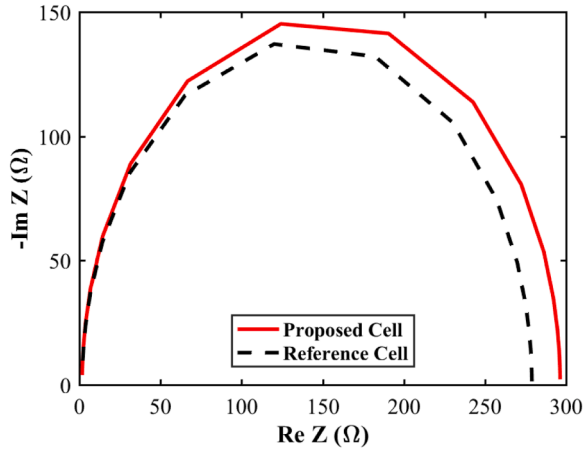


**Fig. 8.** Nyquist plot comparing the proposed cell with Fe-CGST as the secondary absorber layer and the reference cell. The plot illustrates the real resistance (Re Z) versus imaginary resistance (Im Z), showing improved charge transfer and reduced energy losses in the proposed cell.

*Fe-CGST* as a secondary absorber layer to the conventional $Sb_2Se_3$ */CdS/ZnO/AlZnO* structure. In this plot, $1/C^2$, which serves as a measure of the diode's capacitance, is plotted against voltage. This type of plot is especially used for investigating the built-in voltage ($V_{bi}$) and the characteristics of the band bending in solar cells.

The equation governing the Mott-Schottky plot is as follows [50,51]:

$$\frac{1}{C^2} = \frac{2q}{\epsilon A}(V_{\text{bi}}|V) \tag{1}$$

In Eq. (1), C represents the capacitance of the diode, which indicates the ability of the diode to store charge. q is the electric charge, with a value of $1.602 \times 10^{-19}$C, which is the fundamental unit of charge. The symbol $\epsilon$ refers to the dielectric constant of the semiconductor material, which affects how the material responds to an electric field. A represents the area of the diode, which influences the amount of charge that can be stored. $V_{bi}$ is the built-in voltage of the diode, indicating the internal potential difference across the junction. Finally, V is the applied voltage across the diode, which affects the current and capacitance behavior in the system.

For this reason, the built-in potential ($V_{bi}$) is extracted from the most representative quasi-linear region of the Mott–Schottky plot using linear extrapolation, which provides a more physically realistic estimation for complex thin-film solar cells.

In the Mott-Schottky plot, the intercept of the linear region with the voltage axis corresponds to the built-in potential ($V_{bi}$) of the device. This occurs when the depletion width approaches zero, causing the capacitance to become very large and $1/C^2$ to approach zero. Therefore, the onset of the curve along the voltage axis provides a direct indication of the internal electric field and junction properties of the solar cell.

In the proposed cell, which utilizes *Fe-CGST* as a secondary absorber layer, the built-in voltage ($V_{bi}$) is found to be 1.07 V. This is significantly higher than the built-in voltage of the reference cell, which has a $V_{bi}$ of 0.78 V. The difference in $V_{bi}$ indicates an improvement in the internal electric potential and enhanced ability to separate charges in the proposed cells. The increase in $V_{bi}$ in the new structure reflects an improvement in the cell's performance in terms of both efficiency and stability.

This plot directly analyzes the characteristics of the band bending and band alignment in the different solar cell structures. In the proposed cell, *Fe-CGST* as a secondary absorber layer improves the charge separation and increases the built-in voltage, directly impacting the electrical performance of the cell.

Overall, the Mott-Schottky plot provides precise information regarding the electrical properties and band bending stability in both structures, confirming the positive effects of *Fe-CGST* in improving the performance of the solar cells.

In this Fig. 7, the External Quantum Efficiency (EQE) versus wavelength for the proposed cell with *Fe-CGST* as the secondary absorber layer and the conventional cell is compared. The plot illustrates the performance of the solar cells in terms of light absorption across different wavelengths and provides crucial insights into the ability of the cell to capture energy from various parts of the solar spectrum.

In the proposed cell, a significant increase in EQE is observed across a broader range of wavelengths. It is important to note that the improvement in the short-wavelength region (below 600 nm) is not primarily due to increased optical absorption by the Fe-CGST layer, but rather due to enhanced carrier collection efficiency. The incorporation of the Fe-CGST layer improves band alignment and increases the built-in electric field, leading to more efficient separation and transport of photogenerated carriers in the $Sb_2Se_3$ layer. Additionally, reduced recombination losses at the interfaces contribute to improved carrier extraction. As a result, the EQE enhancement in this region reflects improved device physics rather than purely optical effects. This enhancement in EQE is directly correlated with the increase in short-circuit current density ($J_{sc}$), and indirectly contributes to improvements in fill factor (FF) and open-circuit voltage ($V_{oc}$) through reduced recombination and improved charge transport.

This indicates a substantial enhancement in light absorption capability, particularly in the longer-wavelength region (above ~600 nm), where the conventional cell exhibits a significant drop in EQE. In contrast, the conventional cell shows relatively higher EQE in the short-wavelength region (below ~600 nm), but its performance declines rapidly at higher wavelengths. The improved response of the proposed cell in this region is attributed to enhanced spectral utilization, partially enabled by the incorporation of Fe-CGST and intermediate band (IB)-assisted absorption mechanisms.

This difference in EQE between the proposed and conventional cells highlights the effective role of *Fe-CGST* in enhancing light absorption in the longer wavelengths and contributing to the overall improvement in the solar cell's efficiency. By adding *Fe-CGST* as a secondary absorber layer, the new structure is able to capture a wider spectrum of sunlight, directly leading to higher efficiency and better energy conversion.

The results from this plot emphasize that the inclusion of *Fe-CGST* in the proposed cell significantly increases its ability to absorb light, especially in the higher wavelength regions, thereby improving the overall performance of the solar cell.

In Fig. 8, the Nyquist plot for both the proposed cell and the reference cell is presented, with real resistance (Re Z) plotted against imaginary

resistance (Im Z). This plot is extensively used for analyzing the electrical behavior of semiconductor systems, such as solar cells, and is particularly valuable in investigating dynamic phenomena like frequency response and charge transfer resistances.

The Nyquist plot typically represents the complex resistance $Z$, which can be expressed as [52,53]:

$$Z = R + jX \tag{2}$$

where $R$ is the real resistance, $X$ is the imaginary resistance (related to dynamic processes), and $j$ is the imaginary unit. In the context of solar cells, this plot specifically addresses charge transfer resistance and the response of different cell regions to varying frequencies.

For the proposed cell utilizing Fe-CGST as the secondary absorber layer, noticeable changes in the Nyquist response are observed, reflecting modifications in interfacial charge-transfer and recombination processes. In photovoltaic devices, the radius of the semicircle in the Nyquist plot is not solely related to conductivity, but is often associated with recombination resistance and interface-related charge dynamics. In this context, a larger semicircle can indicate higher recombination resistance, which corresponds to suppressed carrier recombination and improved carrier lifetime. Therefore, the behavior observed in the proposed cell is attributed to improved interfacial electronic properties and reduced recombination losses, rather than simply a decrease in total resistance. In contrast, the reference cell exhibits characteristics consistent with higher recombination activity and less efficient charge transport. These differences in impedance response are consistent with the improved photovoltaic performance observed in the proposed structure, including higher open-circuit voltage ($V_{oc}$), enhanced EQE, and increased overall efficiency.

The Nyquist plot analysis also reveals that the proposed cell shows a flatter curve and a shallower slope, confirming higher efficiency and better charge transfer characteristics. These features are critical for achieving high-efficiency solar cells with long-term stability.

Table 2, presents the performance characteristics of the solar cells with varying *Fe-CGST* absorber layer thicknesses. As shown, the open-circuit voltage ($V_{oc}$), short-circuit current density ($J_{sc}$), fill factor (FF), and efficiency ($\eta$) are evaluated for different absorber thicknesses of *Fe-CGST*, specifically at 100 nm, 400 nm, and 700 nm.

The data reveals that the $V_{oc}$ remains relatively constant across the different thicknesses, ranging from 0.7748 V at 100 nm to 0.7758 V at 400 nm, and slightly decreasing to 0.7750 V at 700 nm. This indicates that the open-circuit voltage is not significantly affected by the absorber thickness within this range, suggesting a stable voltage behavior regardless of layer thickness.

The $J_{sc}$ (short-circuit current density) shows a consistent increase with increasing absorber thickness. It rises from 34.28 $mA/cm^2$ at 100 nm to 34.78 $mA/cm^2$ at 700 nm, with the 400 nm thickness showing an intermediate value of 34.51 $mA/cm^2$. This suggests that thicker *Fe-CGST* layers enable greater light absorption, which in turn enhances the current density.

However, the most significant observation is the change in fill factor (FF) and efficiency ($\eta$). The FF and $\eta$ reach their highest values at a 400 nm thickness, with FF at 69.25% and $\eta$ at 18.54%. This indicates that the optimal thickness for maximizing efficiency is 400 nm, where both charge transfer and light absorption are sufficiently balanced, resulting in improved overall performance. The efficiency decreases slightly for both thinner (100 nm) and thicker (700 nm) layers, highlighting the importance of optimizing the absorber thickness for achieving peak performance.

**Table 2**
Comparison of performance characteristics for solar cells with different Fe-CGST absorber layer thicknesses. The highest efficiency (η) and fill factor (FF) are observed at a 400 nm thickness.

| Thickness of *Fe-CGST* (nm) | $V_{oc}$ (V) | $J_{sc}$ ($mA/cm^2$) | FF (%) | $\eta$ (%) |
|---|---|---|---|---|
| 100 | 0.7748 | 34.28 | 68.34 | 18.15 |
| **400** | **0.7758** | **34.51** | **69.25** | **18.54** |
| 700 | 0.7750 | 34.78 | 68.11 | 18.36 |

In summary, the data suggests that a 400 nm thick *Fe-CGST* layer offers the optimal balance of light absorption, charge transfer, and efficiency, making it the best choice for maximizing the performance of *$Sb_2Se_3$ /Fe-CGST* solar cells.

The variation in device performance with Fe-CGST thickness can be explained by the trade-off between optical absorption and charge transport. For thinner layers, insufficient absorption limits carrier generation, leading to lower current density. In contrast, excessively thick layers increase recombination losses and internal resistance, which negatively affect carrier transport and reduce the fill factor.

The optimal thickness of 400 nm represents a balance between these competing effects, resulting in maximum efficiency. The observed trend suggests that the optimal performance lies within an intermediate thickness range (approximately 300–500 nm), where both absorption and carrier transport are effectively optimized.

In Fig. 9, the relationship between open-circuit voltage ($V_{oc}$) and temperature (T) for both the proposed cell (*$Sb_2Se_3$ /Fe-CGST/CdS*) and the reference cell (*$Sb_2Se_3$ /CdS*) is presented. This plot is particularly useful for analyzing the temperature-dependent behavior of the solar cells, especially in terms of their open-circuit voltage under varying environmental conditions.

The open-circuit voltage ($V_{oc}$) as a function of temperature is typically described by a linear relationship according to the Arrhenius equation, which is given by [54,55]:

$$V_{\mathrm{oc}}(T) = V_{\mathrm{oc0}} - \frac{E_a}{k_B}.T \tag{3}$$

In the Eq. (3), $V_{\mathrm{oc}}(T)$represents the open-circuit voltage at temperature $T$, while $V_{\mathrm{oc0}}$ is the open-circuit voltage at a reference temperature. The parameter $E_a$ is the activation energy (measured in eV), which indicates the sensitivity of the open-circuit voltage to temperature changes. $k_B$ is the Boltzmann constant ($8.617 \times 10^{-5}$ eV/K), and $T$ is the temperature in Kelvin. These parameters collectively define the temperature-dependent behavior of the open-circuit voltage in semiconductor materials.

In the proposed cell, which incorporates *Fe-CGST* as the secondary absorber layer, it is evident that $V_{oc}$ decreases with increasing temperature. The rate of this decrease is more pronounced in the proposed cell than in the reference cell, with the activation energy values of $E_a$ = 1.21 eV for the proposed cell and $E_a$ = 0.9 eV for the reference cell. This indicates that the proposed cell is more sensitive to temperature

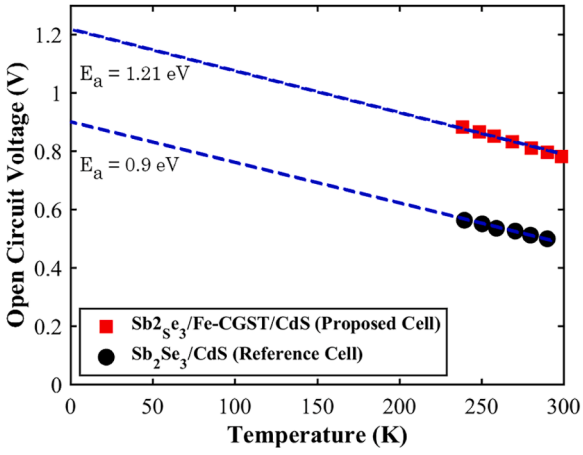


**Fig. 9.** *Temperature dependence of the open-circuit voltage ($V_{oc}$)* for the proposed cell (*$Sb_2Se_3$*/Fe-CGST/CdS) and the reference cell (*$Sb_2Se_3$*/CdS). The activation energy ($E_a$) values are provided, showing how the $V_{oc}$ decreases with increasing temperature for both cell structures.

variations.

The plot demonstrates that the proposed cell with *Fe-CGST* maintains a higher $V_{oc}$ at elevated temperatures compared to the reference cell. However, as the temperature increases, the $V_{oc}$ for both cells decreases. The proposed cell with a higher $E_a$ shows greater temperature dependence, which can be advantageous for optimizing solar cell performance under varying environmental conditions.

The extracted activation energy ($E_a$) provides insight into the dominant recombination mechanism in the device. When $E_a$ approaches the bandgap energy ($E_g$) of the absorber, recombination is primarily dominated by bulk processes, whereas lower Ea values indicate significant interface-related recombination.

In the proposed device, the $E_a$ value (≈ 1.21 eV) is close to the bandgap of $Sb_2Se_3$ (≈ 1.1 eV), suggesting reduced interface recombination and improved junction quality. In contrast, the lower $E_a$ value in the reference cell (≈ 0.9 eV) indicates higher recombination losses at the interfaces.

Moreover, the higher $E_a$ in the proposed device is associated with a lower saturation current density ($J_o$), which contributes to the improved open-circuit voltage ($V_{oc}$). These results confirm that the proposed structure exhibits superior electronic quality and reduced recombination losses.

In Fig. 10, the capacitance (C) as a function of frequency (f) is presented for both the proposed cell ($Sb_2Se_3$/Fe-CGST/CdS) and the reference cell ($Sb_2Se_3$/CdS). The plot illustrates the capacitance behavior across different frequency ranges for each cell structure.

The capacitance in semiconductors is commonly modeled as a function of frequency and temperature. The general relationship for the capacitance of a diode can be described by the following equation [14, 34]:

$$C(f) = \frac{C_0}{(1|j2\pi f\tau)^n} \tag{4}$$

where C(f) represents the capacitance at a given frequency f, $C_o$ is the static capacitance, τ is the relaxation time associated with charge dynamics, and n reflects the dispersion behavior of the system.

In the reference cell, the capacitance is higher at lower frequencies and decreases sharply with increasing frequency, eventually approaching a nearly constant value. This behavior is associated with charge storage and carrier response limitations at higher frequencies.

In the proposed cell, which incorporates Fe-CGST as the secondary absorber layer, the capacitance remains relatively constant over a wider low-to-mid frequency range and decreases more gradually at higher frequencies. This behavior indicates that the capacitance response is largely dominated by the geometrical capacitance and the overall dielectric properties of the multilayer structure.

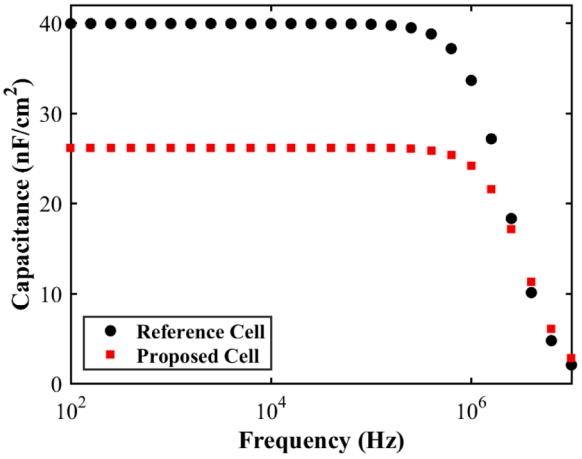


**Fig. 10.** Capacitance vs frequency for the reference cell and proposed cell, highlighting the improved stability of the proposed cell with Fe-CGST as the secondary absorber layer.

In thin-film solar cells, the capacitance in such regimes can be approximated by the relation $C = \varepsilon A/d$, where ε is the effective dielectric permittivity, A is the device area, and d is the total electrically active thickness of the structure. Accordingly, the incorporation of the Fe-CGST layer increases the overall thickness of the absorber region, which leads to a reduction in capacitance, consistent with the inverse relationship between capacitance and thickness.

This interpretation is consistent with previously reported studies, where geometrical capacitance has been used to estimate absorber thickness in thin-film photovoltaic devices [49]. It should be noted that, in the present work, the capacitance analysis is primarily used to qualitatively assess structural and dielectric effects rather than to extract an exact thickness value.

Overall, the observed capacitance behavior confirms that the differences between the proposed and reference structures are strongly influenced by variations in effective thickness and dielectric response introduced by the additional Fe-CGST layer.

In Fig. 11(a), illustrate the 0.5 $\mu$m $Sb_2Se_3$ absorber, the proposed cell demonstrates a superior performance with $V_{oc}$ = 0.86 V, $J_{sc}$ = 27.70 $mA/cm^2$, FF = 69.09%, and $\eta$ = 16.49%, outperforming the reference cell with $V_{oc}$ = 0.48 V, $J_{sc}$ = 24.76 $mA/cm^2$, FF = 68.05%, and $\eta$ = 8.10%. This improvement is attributed to the inclusion of *Fe-CGST* as a secondary absorber layer, which enhances light absorption and overall cell performance.

Fig. 11(b) shows the 1 $\mu$m $Sb_2Se_3$ absorber, the proposed cell continues to show improved performance, with $V_{oc}$ = 0.81 V, $J_{sc}$ = 32.11 $mA/cm^2$, FF = 70.71%, and $\eta$ = 18.40%, compared to the reference cell with $V_{oc}$ = 0.48 V, $J_{sc}$ = 30.87 $mA/cm^2$, FF = 67.18%, and $\eta$ = 10.12%. This indicates that the *Fe-CGST* layer further improves the efficiency of the solar cell.

The most significant observation is made in the 2.6 $\mu$m $Sb_2Se_3$ absorber (Fig. 11(c)), where the proposed cell exhibits the highest efficiency ($\eta$) and fill factor (FF), with $V_{oc}$ = 0.77 V, $J_{sc}$ = 34.50 $mA/cm^2$, FF = 69.25%, and $\eta$ = 18.54%. This is the optimal thickness for the *Fe-CGST* layer, as it provides the best balance between charge transfer and light absorption. The reference cell shows $V_{oc}$ = 0.49 V, $J_{sc}$ = 34.23 $mA/cm^2$, FF = 66.22%, and $\eta$ = 11.13%, reflecting a significantly lower efficiency. Finally, in Fig. 11 (d), the 3 $\mu$m $Sb_2Se_3$ absorber is shown, the proposed cell continues to perform well with $V_{oc}$ = 0.77 V, $J_{sc}$ = 34.10 $mA/cm^2$, FF = 68.86%, and $\eta$ = 18.40%. The reference cell shows similar $J_{sc}$, but a lower $V_{oc}$, indicating that *Fe-CGST* continues to provide improvements in the proposed cell's performance. Overall, the proposed cell consistently outperforms the reference cell across all absorber thicknesses, with the 2.6 $\mu$m thickness offering the highest efficiency and fill factor, demonstrating the *Fe-CGST* layer's significant contribution to improving solar cell performance.

To rigorously evaluate the intrinsic photovoltaic capability of Fe-CGST and to clearly establish its functional role within the proposed architecture, additional simulations were performed by considering Fe-CGST as a standalone absorber in a single-junction configuration, i.e., without the $Sb_2Se_3$ layer. The resulting current density–voltage (J–V) characteristics and external quantum efficiency (EQE) spectra are presented in Fig. 12(a) and (b), respectively, for Fe-CGST-only devices with varying absorber thicknesses (0.8–2.0 μm), and are directly compared with the proposed dual-absorber structure.

As observed in Fig. 12(a), the Fe-CGST-only devices exhibit relatively high open-circuit voltage ($V_{oc}$), which can be attributed to the wide bandgap of Fe-CGST (~1.9 eV). However, despite this advantage, the short-circuit current density ($J_{sc}$) remains significantly lower than that of the proposed dual-absorber device, resulting in a substantially reduced overall power conversion efficiency. This limitation arises from the inability of the wide-bandgap absorber to effectively harvest lower-energy photons from the solar spectrum.

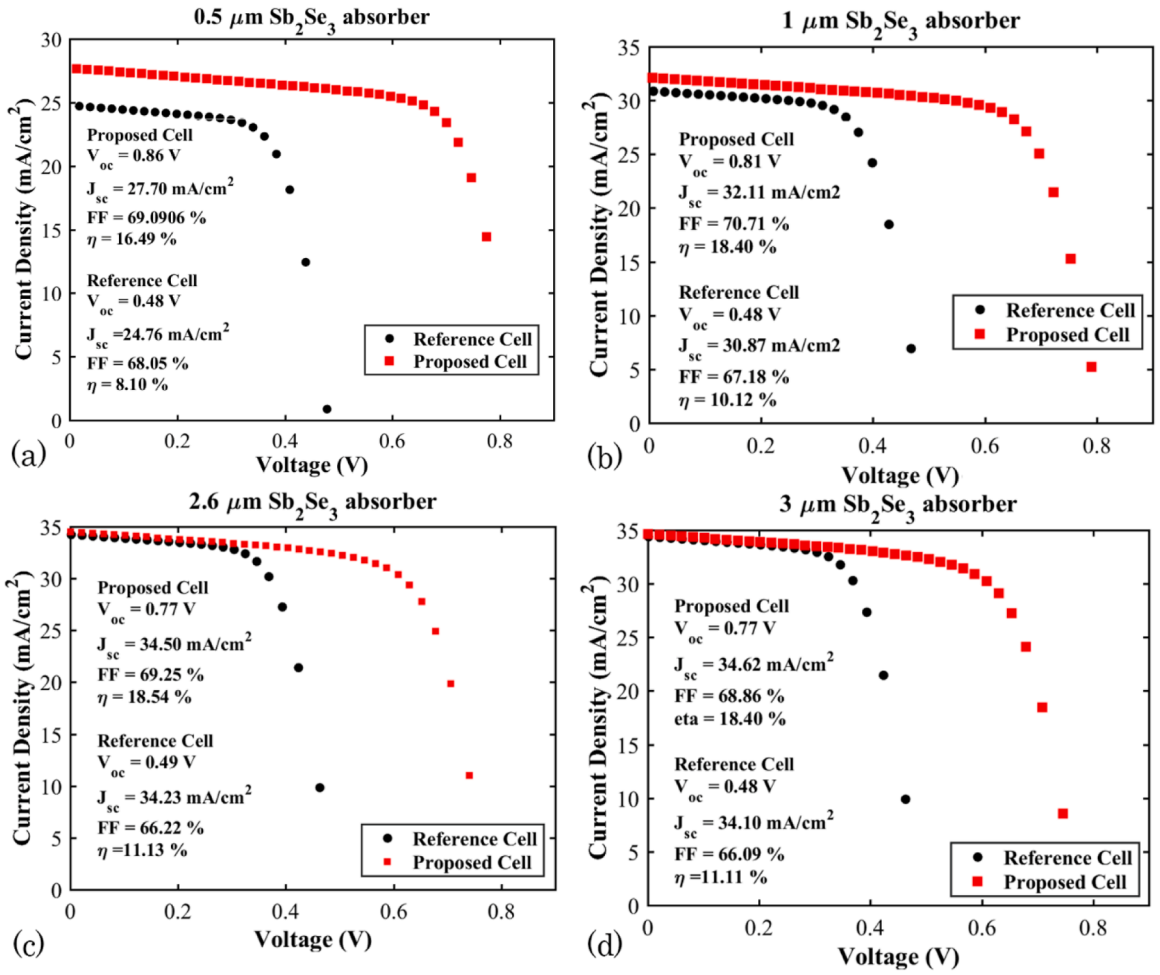


**Fig. 11.** the current density ($J_{sc}$) and open-circuit voltage ($V_{oc}$) are compared for the proposed cell ($Sb_2Se_3$/Fe-CGST/CdS) and the reference cell ($Sb_2Se_3$/CdS) with varying $Sb_2Se_3$ absorber thicknesses. (a), 0.5 $\mu$m, (b), 1 $\mu$m, (c), 2.6 $\mu$m, and (d), 3 $\mu$m.

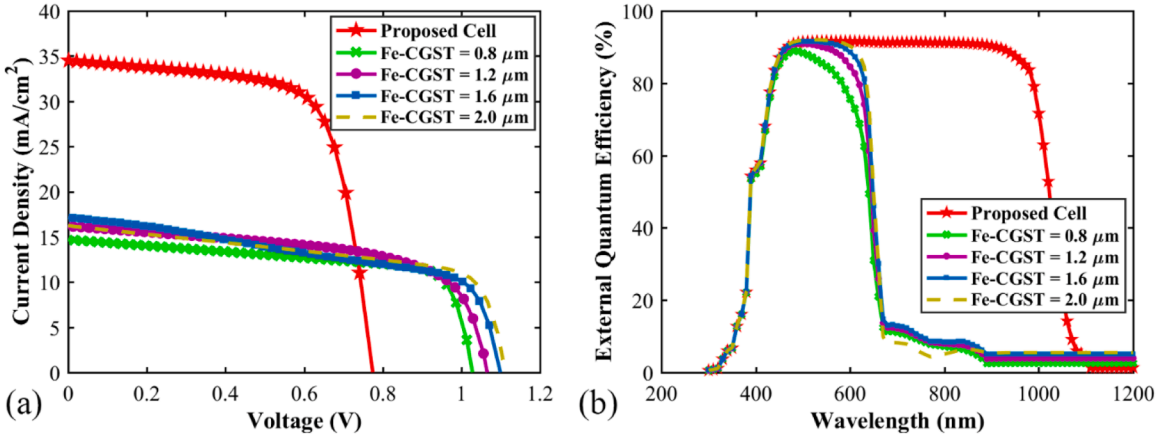


**Fig. 12.** Comparison of the photovoltaic behavior of the proposed dual-absorber cell and Fe-CGST-only single-junction cells with different Fe-CGST thicknesses: (a), J–V characteristics and (b), EQE spectra. The results show that Fe-CGST alone yields relatively low current density and limited spectral response, confirming that its primary role in the present work is as a complementary secondary absorber rather than a standalone absorber.

This behavior is further supported by the EQE spectra (in Fig. 12(b)), where the Fe-CGST-only devices display a relatively narrow spectral response. As seen in the figure, the quantum efficiency is mainly confined to the short-wavelength region, followed by a pronounced decline at longer wavelengths. In contrast, the proposed dual-absorber structure demonstrates a much broader spectral response extending into the visible and near-infrared regions, owing to the contribution of the $Sb_2Se_3$ layer. The absence of this extended response in the Fe-CGST-only configuration indicates that a significant portion of the solar spectrum remains unutilized.

From a device physics perspective, the relatively high $V_{oc}$ observed in Fe-CGST-only cells can be explained by the reduced intrinsic carrier

concentration and lower saturation current density ($J_0$) associated with wide-bandgap materials. However, this benefit is fundamentally offset by the severe limitation in photogenerated current, leading to poor overall device performance. This trade-off reflects the intrinsic limitation of wide-bandgap absorbers when employed in single-junction configurations.

Furthermore, the thickness-dependent trends indicate that increasing the Fe-CGST thickness does not effectively compensate for the limited spectral absorption. While thicker layers provide only marginal improvement in photon absorption, they simultaneously introduce increased recombination losses and carrier transport limitations, which further degrade device performance. This confirms that the performance bottleneck is governed primarily by the material bandgap rather than the absorber thickness alone.

Importantly, these results clearly demonstrate that Fe-CGST is not intended to function as an efficient standalone absorber in this study. Instead, its primary role is to act as a complementary wide-bandgap absorber within a dual-absorber configuration. When integrated with $Sb_2Se_3$, Fe-CGST enhances device performance through multiple synergistic mechanisms, including improved spectral utilization, intermediate-band-assisted sub-bandgap absorption, and enhanced charge separation. Overall, the comparative analysis provides clear evidence that the superior performance of the proposed device originates from the cooperative interaction between the two absorbers. This dual-absorber strategy effectively overcomes the intrinsic limitations of wide-bandgap materials and results in significantly improved photovoltaic performance.

Table 3, compares the open-circuit voltage ($V_{oc}$), short-circuit current density ($J_{sc}$), fill factor (FF), and efficiency ($\eta$) for both simulation results and experimental studies across various research cases. The data shows that the simulation results for the proposed cell with *Fe-CGST* as the secondary absorber layer exhibit a significant performance advantage, with a $V_{oc}$ of 0.77 V, $J_{sc}$ of 34.50 $mA/cm^2$, FF of 69.25%, and an efficiency ($\eta$) of 18.54%. This indicates the optimal performance predicted by the simulation, highlighting the potential of the *Fe-CGST* layer in enhancing light absorption and charge transfer in the solar cell structure.

In contrast, the experimental results show notable differences in performance. The highest-performing experimental study (Ref. [11]) reports a $V_{oc}$ of 0.48 V, $J_{sc}$ of 30.86 $mA/cm^2$, FF of 67.19%, and $\eta$ of 10.12%, which is significantly lower than the simulation values. This discrepancy between experimental and simulated $V_{oc}$ and η could be attributed to various practical factors such as material defects, fabrication variations, or environmental conditions during testing, which can impact the efficiency of real-world devices.

Other experimental studies show even lower performance. For example, the study in [18] reports a $V_{oc}$ of 0.38 V, $J_{sc}$ of 26.24 $mA/cm^2$, FF of 57.82%, and $\eta$ of 5.95%, which further highlights the challenges in achieving high efficiency in practical cells compared to theoretical models. Similarly, the [56] study presents a $V_{oc}$ of 0.57 V, $J_{sc}$ of 10.24 $mA/cm^2$, FF of 55.33%, and $\eta$ of 3.22%, showing even lower performance, likely due to suboptimal material properties or fabrication methods. The [19] study reports a $V_{oc}$ of 0.43 V, $J_{sc}$ of 25.50 $mA/cm^2$, FF of 59.33%, and $\eta$ of 6.51%, still far below the simulation results.

The wide range of experimental results emphasizes the complexities in translating theoretical designs into practical, high-performance solar cells. While the simulation suggests that the *Fe-CGST* secondary absorber layer can achieve 18.54% efficiency, the experimental results consistently show lower efficiency and voltage values, reflecting real-world limitations. These discrepancies highlight the need for further optimization in the fabrication process, material quality, and cell design to bring experimental performance closer to the predicted simulation results.

**Table 3**
Comparison of $V_{oc}$, $J_{sc}$, Fill Factor (FF), and Efficiency ($\eta$) values from both experimental and simulation studies.

| Research Case | $V_{oc}$ (V) | $J_{sc}$ ($mA/cm^2$) | FF (%) | $\eta$ (%) | Reference |
|---|---|---|---|---|---|
| Simulation | 0.77 | 34.50 | 69.25 | 18.54 | This work |
| Experimental | 0.48 | 30.86 | 67.19 | 10.12 | [11] |
| Experimental | 0.38 | 26.24 | 57.82 | 5.95 | [18] |
| Experimental | 0.57 | 10.24 | 55.33 | 3.22 | [56] |
| Experimental | 0.43 | 25.50 | 59.33 | 6.51 | [19] |

In conclusion, the comparison presented in Table 3, underscores the potential of the *Fe-CGST* secondary absorber layer in enhancing the performance of $Sb_2Se_3$ based solar cells. However, the differences between simulation and experimental data emphasize the challenges in material synthesis, device fabrication, and environmental factors that influence the real-world efficiency of solar cells. Further research and development are needed to bridge the gap between theoretical predictions and practical solar cell performance, particularly in optimizing light absorption and charge transfer efficiency.

## 5. Conclusions

This study demonstrates that incorporating Fe-doped $CuGa(S,Te)_2$ (Fe-CGST) as a secondary absorber layer significantly enhances the performance of $Sb_2Se_3$ -based solar cells. Through systematic thickness optimization, the optimal configuration (2.6 μm $Sb_2Se_3$ and 400 nm Fe-CGST) achieves a maximum efficiency of 18.54%.

The performance improvement is attributed to multiple synergistic effects, including enhanced spectral utilization, intermediate band (IB)-assisted sub-bandgap absorption, improved band alignment, and reduced recombination losses. The presence of the IB plays a key role in increasing carrier generation, while the optimized thickness ensures a balance between light absorption and charge transport.

Furthermore, optoelectronic analyses confirm improved charge transfer dynamics, higher built-in potential, and enhanced carrier collection efficiency. These results highlight the potential of combining dual-absorber architecture with intermediate band engineering as an effective strategy for developing high-efficiency thin-film solar cells.

## CRediT authorship contribution statement

**Mehdi Mousavi-Kamazani:** Validation, Supervision, Data curation, Conceptualization. **Mohammad Danaie:** Writing – review & editing, Supervision, Project administration, Formal analysis, Conceptualization. **Danial Keighobadi:** Writing – original draft, Software, Investigation, Data curation, Conceptualization. **Ali Asghar Orouji:** Writing – review & editing, Validation, Software.

## Ethical approval statement

The authors confirm that the submitted paper has not been submitted to any other journal and that this version is original and has not been published elsewhere. Additionally, all listed authors affirm the integrity of the study, data, information, and analyses, ensuring that no manipulations have been made. Furthermore, we confirm that no other individuals meet the authorship criteria for this paper beyond those listed as authors.

## Declaration of Generative AI and AI-assisted technologies in the writing process

The authors declare that AI tools were used to improve the English content of this paper.

## Funding

The authors declare that no funds, grants, or financial support were received for the preparation of this manuscript.

## Declaration of Competing Interest

The authors declare that they have no known competing financial interests or personal relationships that could have appeared to influence the work reported in this paper.

## Data availability

Data will be made available on request.

## References


[1] N. Asim, et al., A review on the role of materials science in solar cells, Renew. Sustain. Energy Rev. 16 (8) (2012) 5834–5847.
[2] P. Choubey, A. Oudhia, R. Dewangan, A review: solar cell current scenario and future trends, Recent Res. Sci. Technol. 4 (8) (2012).
[3] T.D. Lee, A.U. Ebong, A review of thin film solar cell technologies and challenges, Renew. Sustain. Energy Rev. 70 (2017) 1286–1297.
[4] F. Mujtahid, et al., Review effect of various types of dyes and structures in supporting performance of dye-sensitized solar cell TiO2-based nanocomposites, Int. J. Energy Res. 46 (2) (2022) 726–742.
[5] K. Machkih, R. Oubaki, M. Makha, A review of CIGS thin film semiconductor deposition via sputtering and thermal evaporation for solar cell applications, Coatings 14 (9) (2024) 1088.
[6] W. Akram, et al., A review of life cycle assessment and sustainability analysis of perovskite/Si tandem solar cells, RSC Sustain. 3 (1) (2025) 21–36.
[7] G. Tang, et al., A Review on recent advances in flexible perovskite solar cells, Sol. RRL 9 (5) (2025) 2400844.
[8] A. Karaca, et al., Characterization of Cu (In, Ga)(Te, S) 2 thin films grown on stainless steel foil substrates, J. Phys. D Appl. Phys. 56 (19) (2023) 195302.
[9] A. Çiriş, et al., Effect of CdS and CdSe pre-treatment on interdiffusion with CdTe in CdS/CdTe and CdSe/CdTe heterostructures, Mater. Sci. Semicond. Process. 128 (2021) 105750.
[10] Y. Singh, et al., Sb2Se3 heterostructure solar cells: techniques to improve efficiency, Sol. Energy 249 (2023) 174–182.
[11] Z. Duan, et al., Sb2Se3 thin-film solar cells exceeding 10% power conversion efficiency enabled by injection vapor deposition technology, Adv. Mater. 34 (30) (2022) 2202969.
[12] C. Chen, K. Li, J. Tang, Ten years of Sb2Se3 thin film solar cells, Sol. RRL 6 (7) (2022) 2200094.
[13] H. Cai, et al., Interfacial engineering towards enhanced photovoltaic performance of Sb2Se3 solar cell, Adv. Funct. Mater. 32 (46) (2022) 2208243.
[14] G. Wu, et al., Study of antimony selenide hole-transport material for Mo/Sb2Se3/MAPbI3/C60/GZO/Ag heterojunction planar solar cells, Surf. Coat. Technol. 405 (2021) 126550.
[15] K. Maurya, V. Singh, Sb2Se3 versus Sb2S3 solar cell: a numerical simulation, Sol. Energy 228 (2021) 540–549.
[16] Z.-Q. Li, M. Ni, X.-D. Feng, Simulation of the Sb2Se3 solar cell with a hole transport layer, Mater. Res. Express 7 (1) (2020) 016416.
[17] X. Wang, et al., Interfacial engineering for high efficiency solution processed Sb2Se3 solar cells, Sol. Energy Mater. Sol. Cells 189 (2019) 5–10.
[18] L. Wang, et al., Stable 6%-efficient Sb2Se3 solar cells with a ZnO buffer layer, Nat. Energy 2 (4) (2017) 1–9.
[19] C. Chen, et al., 6.5% certified efficiency Sb2Se3 solar cells using PbS colloidal quantum dot film as hole-transporting layer, ACS Energy Lett. 2 (9) (2017) 2125–2132.
[20] G. Yadav, M. Ahmaruzzaman, CdIn2S4-based advanced composite materials: structure, properties, and applications in environment and energy–A concise review, Inorg. Nano-Met. Chem. 55 (2) (2025) 122–136.
[21] D. Xu, et al., Record-efficiency inverted CsPbI3 perovskite solar cells enabled by rearrangement and hydrophilic modification of SAMs. Adv. Funct. Mater. 35 (2) (2025) 2412946.
[22] M. Minbashi, et al., Comparison of theoretical and experimental results for band-gap-graded CZTSSe solar cell, Curr. Appl. Phys. 17 (10) (2017) 1238–1243.
[23] M. Danaie, A. Geravand, Design of low-cross-talk metal–insulator–metal plasmonic waveguide intersections based on proposed cross-shaped resonators, J. Nanophoton. 12 (4) (2018), 046009–046009.
[24] Y. Gong, et al., Elemental de-mixing-induced epitaxial kesterite/CdS interface enabling 13%-efficiency kesterite solar cells, Nat. Energy 7 (10) (2022) 966–977.
[25] M. Jost, et al., Perovskite/CIGS tandem solar cells: from certified 24.2% toward 30% and beyond, ACS Energy Lett. 7 (4) (2022) 1298–1307.
[26] Y. An, et al., Balancing carrier transport in interconnection layer for efficient perovskite/organic tandem solar cells, Nat. Commun. 16 (1) (2025) 1–11.
[27] X. Ma, et al., Facile fabrication of CdIn2S4/TiO2 heterojunction for enhanced solar light efficient CO2 reduction, Front. Chem. Sci. Eng. 18 (9) (2024) 105.
[28] T. Wu, et al., The main progress of perovskite solar cells in 2020–2021, Nano-Micro Lett. 13 (1) (2021) 152.
[29] A. Ait Abdelkadir, et al., Numerical simulation and optimization of n-Al-ZnO/n-CdS/p-CZTSe/p-NiO (HTL)/Mo solar cell system using SCAPS-1D, Results Opt. 8 (2022) 100257.
[30] S. Yılmaz, et al., Enhancement of the response speed of CIGS-based photodetector by Te-doping, Sens. Actuators A Phys. 377 (2024) 115691.
[31] A. El Khalfi, et al., Dual-absorber solar cell design and simulation based on Sb2Se3 and CZTGSe for high-efficiency solar cells, Langmuir 40 (39) (2024) 20352–20367.
[32] B.K. Mondal, S.K. Mostaque, J. Hossain, Theoretical insights into a high-efficiency Sb2Se3-based dual-heterojunction solar cell, Heliyon 8 (3) (2022).
[33] K. Maurya, V. Singh, Sb2Se3/CZTS dual absorber layer based solar cell with 36.32% efficiency: a numerical simulation, J. Sci. Adv. Mater. Devices 7 (2) (2022) 100445.
[34] T.S. Natarajan, R.J. Tayade, Direct dual CaIn2S4/Bi2WO6 semiconductor nanocomposites with efficient inter-cross-sectional charge carrier transfer for enhanced visible light photocatalysis, J. Nanopart. Res. 23 (6) (2021) 127.
[35] A.S. Al-Ezzi, M.N.M. Ansari, Photovoltaic solar cells: a review, Appl. Syst. Innov. 5 (4) (2022) 67.
[36] S. Yılmaz, et al., Comparative analysis of chloride-treated ZnTe films in photodetector devices, Mater. Sci. Semicond. Process. 198 (2025) 109733.
[37] S. Yılmaz, et al., Improvement in performance of SnSe-based photodetectors via post deposition sulfur diffusion, Sens. Actuators A Phys. 372 (2024) 115348.
[38] S. Yılmaz, et al., Fabrication and characterization of self-powered SnO2/CdTe1-xSex/CdTe photodetectors, J. Mater. Sci. Mater. Electron. 35 (36) (2024) 2300.
[39] A. Çiriş, et al., Processing CdS-and CdSe-containing window layers for CdTe solar cells, J. Phys. D Appl. Phys. 54 (21) (2021) 215103.
[40] A. Çiriş, et al., Deposition of CdSeTe alloys using CdTe—CdSe mixed powder source material in a close-space sublimation process, J. Mater. Sci. Mater. Electron. 32 (7) (2021) 9685–9693.
[41] K. Vijayan, et al., A novel approach for designing a sub-bandgap in CuGa (S, Te) 2 thin films assisted with numerical simulation of solar cell devices for photovoltaic application, ACS Omega 8 (25) (2023) 22414–22427.
[42] A.S. Bati, et al., Next-generation applications for integrated perovskite solar cells, Commun. Mater. 4 (1) (2023) 2.
[43] J. Zhu, et al., Interfacial charge and surface defect regulation for high-efficiency CdIn2S4-based photoanodes, Appl. Surf. Sci. 601 (2022) 154188.
[44] K.O. Brinkmann, et al., Perovskite–organic tandem solar cells, Nat. Rev. Mater. 9 (3) (2024) 202–217.
[45] P. Choubey, R. Verma, M. Basu, Passivation of Surface States in CdIn2S4 via Type II Heterostructure for Boosting Photoelectrochemical Water Splitting Reaction, ACS Appl. Energy Mater. 7 (20) (2024) 9382–9393.
[46] M.K. Omrani, et al., Improve the performance of CZTSSe solar cells by applying a SnS BSF layer, Solid-State Electron. 141 (2018) 50–57.
[47] Y. Rong, et al., Challenges for commercializing perovskite solar cells, Science 361 (6408) (2018) eaat8235.
[48] D. Keighobadi, M. Mousavi-Kamazani, M. Danaie, Optimizing Sb2Se3 solar cells with CdIn2S4 buffer for high-efficiency and stability: a comprehensive analysis, Mater. Des. (2026) 115912.
[49] J.V. Li, et al., A method to measure resistivity, mobility, and absorber thickness in thin-film solar cells with application to CdTe devices, Sol. Energy Mater. Sol. Cells 94 (12) (2010) 2073–2077.
[50] N. Nikfar, N. Memarian, Theoretical study on the effect of electron transport layer parameters on the functionality of double-cation perovskite solar cells, Optik 258 (2022) 168932.
[51] F. Shahnooshi, A.A. Orouji, A. Abbasi, Enhanced performance of Graphene/AlGaAs/GaAs heterostructure Schottky solar cell using AlGaAs drainage, J. Mater. Sci. Mater. Electron. 33 (7) (2022) 4617–4627.
[52] J.J. Yoo, S.S. Shin, J. Seo, Toward efficient perovskite solar cells: progress, strategies, and perspectives, ACS Energy Lett. 7 (6) (2022) 2084–2091.
[53] T. Chargui, et al., Experimental and numerical study of the CIGS/CdS heterojunction solar cell, Opt. Mater. 140 (2023) 113849.
[54] S. Khatoon, et al., Simulation study of CsPbIxBr1-x and MAPbI3 heterojunction solar cell using SCAPS-1D, Sol. Energy 254 (2023) 137–157.
[55] M.A.H. Pappu, et al., Design of n-CdS/p-CuInTe2/p+-MoS2 thin film solar cell with a power conversion efficiency of 34.32, Opt. Contin. 2 (4) (2023) 942–955.
[56] H. Deng, et al., Efficient and stable TiO2/Sb2S3 planar solar cells from absorber crystallization and Se-atmosphere annealing, Mater. Today Energy 3 (2017) 15–23.